

34 ANSEICCA: a Python package for seismic ambient noise source
35 inversion by cross-correlation modelling

36 Arjun Datta^a, Aileni Mahesh^a

37 ^aDepartment of Earth and Climate Science, Indian Institute of Science Education and Research, Pune, India

38
39
40
41 **ARTICLE INFO**

42 *Keywords:*
43 Open-source
44 Python
45 Seismic ambient noise
46 Cross-correlation modelling
47 Waveform inversion
48 mpi4py
49 Devito
50
51
52
53
54
55

ABSTRACT

We present ANSEICCA, an open-source package for forward and inverse modelling of seismic ambient noise cross-correlations at local scales, where the effects of Earth's sphericity are negligible. The package implements a nonlinear finite-frequency inversion technique wherein measurements of cross-correlation energy are used to invert for the spatial distribution of ambient noise sources, under the assumption of a fixed Earth structure model. It is seamlessly integrated with other open-source Python packages for seismic wave propagation modelling, including a C-based numerical solver for acoustic modelling in 2-D media. It is a unique package insofar as the inversion is based on finite-frequency sensitivity kernels, but executed without the adjoint method. Instead, speed and computational efficiency are achieved by parallelising the code. Moreover, the Hessian-based optimization ensures convergence in a relatively small number of iterations (≈ 10), compared to purely gradient-based methods. We introduce the structure of the package in detail, describing both the serial and parallel versions of the code. Performance benchmarks show that ANSEICCA affords compute times of the order of a few minutes per iteration of inversion, with typical local-scale seismic array geometries.

56
57 **CRedit authorship contribution statement**

58 **Arjun Datta:** Conceptualization, Methodology, Software, Writing - main draft. **Aileni Mahesh:** Software testing
59 and benchmarking, Writing - figures and tables, software manual.

60
61 *This is a non peer reviewed pre-print submitted to EarthArxiv. It is being considered for publication in Computers and*
62 *Geosciences.*

63
ORCID(s): 0000-0002-8249-9399 (A. Datta)

64 1. Introduction

65 The ambient seismic field, or seismic ambient noise, is now one of the mainstays of seismological research. In-
66 terferometric techniques such as auto- and cross-correlations, are commonly used to extract meaningful signals from
67 ambient noise recordings. Most applications exploit the assumption of Green's function retrieval from inter-station
68 cross-correlations (Lobkis and Weaver, 2001; Shapiro and Campillo, 2004). In recent years, recognition of the limi-
69 tations of this approach (e.g. Halliday and Curtis, 2008; Yao and van der Hilst, 2009; Kimman and Trampert, 2010;
70 Fichtner, 2014) has prompted a parallel research track of interferometry using full-wave theory or 'interferometry with-
71 out Green's function retrieval' (e.g. Fichtner et al., 2017; Fichtner and Tsai, 2019). In this unconventional approach,
72 ambient noise cross-correlations are self-contained seismic observables which can be modelled through source and
73 structure parameters, similar to traditional seismic observables from earthquake or explosive sources. This paper is
74 concerned with using full-wave interferometry to invert for the spatial distribution of ambient noise sources.

75 Very few open-source codes for full-wave interferometry are available, perhaps reflecting its inherent mathematical
76 and computational complexity compared to the conventional approach of Green's function retrieval. SPEC3D
77 (Tromp et al., 2010) contains an implementation of noise cross-correlations and sensitivity kernels, but is cumbersome
78 to use for inversion, as noted by Ermert et al. (2020). With specific regard to noise source inversion, where a fixed Earth
79 structure model (of density and seismic velocities) is assumed, the only dedicated open-source code we are aware of, is
80 the Python package called `noisi` (Ermert et al., 2020). `noisi` was developed for regional to global scale applications
81 (e.g. Igel et al., 2021). Here we present ANSEICCA, an ambient noise source inversion package, also in Python, but
82 tailor made for local-scale applications. Ambient noise studies at the local scale can be used for tomography, but are
83 also important for other applications such as the analysis of site effects (e.g. Roten et al., 2006; Denolle et al., 2013;
84 Bowden et al., 2015). Due to the relatively lower demands of local-scale seismic modelling, ANSEICCA espouses
85 a different computational philosophy than `noisi`. Rather than utilizing pre-computed databases of Green's functions
86 to model seismic wave propagation from ambient noise sources, it generates these on the fly. Additionally, there are
87 technical differences pertaining to the particular form of forward and inverse modelling used, as also the manner in
88 which inversion is implemented.

89 ANSEICCA can be a useful tool for seismologists interested in the rigorous modelling and inversion of ambient
90 noise cross-correlations. It may be particularly helpful to new researchers or those from other fields who wish to
91 venture into the realm of full-wave seismic interferometry, but are deterred by the dense mathematical formulation of
92 adjoint methods. ANSEICCA harnesses the power of full-wave theory and finite frequency sensitivity kernels, without
93 using adjoint techniques to compute the kernels (see Datta et al., 2023). This theoretical simplicity comes at the cost
94 of computational efficiency — individual source sensitivity kernels need to be computed for each receiver pair, so the
95 compute time increases non-linearly with the number of receivers involved. To alleviate this issue, we parallelise the

96 code using *mpi4py* (Dalcín et al., 2005). The parallelised implementation makes ANSEICCA efficient and practically
 97 useful for realistic applications. Finally, we note that whilst ANSEICCA is primarily intended to be an inversion tool, it
 98 can, like *noisi*, also be used simply for cross-correlation modelling (e.g. Malkoti et al., 2021). This is useful to study
 99 the influence of noise sources on ground motion auto-correlations, or on specific measurements such as attenuation
 100 (e.g. Stehly and Boué, 2017) or Rayleigh wave ellipticity (Malkoti et al., 2021). Moreover, it can be used to assess the
 101 quality of empirical Green’s functions retrieved from ambient noise cross-correlations, for various source scenarios
 102 and heterogeneous Earth models.

103 The first version of ANSEICCA (Datta et al., 2019) had limited applicability as it could only handle a homogeneous
 104 acoustic medium. Since then the code has been refined as well as advanced, to incorporate increasing levels of forward
 105 modelling rigour, culminating in the recent work by Datta et al. (2023), who incorporated 2-D acoustic modelling.
 106 The current version of ANSEICCA, presented in this paper, incorporates three different forward modelling regimes,
 107 all in one code package. Although the theoretical foundations of each technique advancement have been documented
 108 in past papers, this paper focuses on the code and provides a comprehensive overview. We first present the modelling
 109 methods and their implementation (Section 2), then describe the code in detail (Section 3), and finally provide some
 110 performance benchmarks (Section 4).

111 2. Modelling methods

112 This is an inversion package for estimating seismic ambient noise source distributions. It requires a forward model
 113 for interstation cross-correlations arising from distributed noise sources, and inversion is performed using sensitivity
 114 kernels for cross-correlation amplitudes/energy. Both the forward and inverse modelling schemes are described in this
 115 section, with a focus on computation and code implementation.

116 2.1. Forward modelling

117 Given a spatial distribution, $\sigma(\mathbf{x})$, of ambient noise sources with power spectrum $P(\omega)$, the cross-correlation
 118 $C(\mathbf{x}_A, \mathbf{x}_B)$ of ambient noise recorded at receiver locations \mathbf{x}_A and \mathbf{x}_B is modelled in the frequency domain using the
 119 medium Green’s function G , as:

$$C(\mathbf{x}_A, \mathbf{x}_B; \omega) = P(\omega) \int d^2\mathbf{x} G^*(\mathbf{x}_A, \mathbf{x}; \omega) G(\mathbf{x}_B, \mathbf{x}; \omega) \sigma(\mathbf{x}), \quad (1)$$

in the scalar/acoustic scenario (Datta et al., 2019, 2023), and as

$$C_{pq}(\mathbf{x}_A, \mathbf{x}_B; \omega) = P(\omega) \int d^2\mathbf{x} G_{pi}^*(\mathbf{x}_A, \mathbf{x}; \omega) G_{qi}(\mathbf{x}_B, \mathbf{x}; \omega) \sigma(\mathbf{x}), \quad (2)$$

120 in the elastic scenario (Malkoti et al., 2021; Datta, 2023). In both the above equations, the asterisk denotes complex
 121 conjugation. The Green's function as well as cross-correlation are scalar quantities in Equation (1), but tensors in
 122 Equation (2), where subscripts p and q denote the components of motion at receivers \mathbf{x}_A and \mathbf{x}_B respectively, while
 123 subscript i refers to the direction of impulsive force at the source location \mathbf{x} .

124 The forward model represented by equations (1) and (2) corresponds to ensemble-averaging of spatially uncor-
 125 related noise sources (e.g. Tromp et al., 2010; Sager et al., 2020; Fichtner and Tsai, 2019), subject to the following
 126 additional assumptions:

- 127 (i) The power-spectral density of the noise sources, $S(\mathbf{x}, \omega)$, is separable into position-dependent, and frequency-
 128 dependent terms, i.e. $S(\mathbf{x}, \omega) = P(\omega)\sigma(\mathbf{x})$. In other words, noise sources everywhere have the same spectral
 129 shape $P(\omega)$, only their strength is modulated by the function $\sigma(\mathbf{x})$.
- 130 (ii) In the elastic case, it is assumed that all noise sources are point forces acting in the same direction, so that S is
 131 still a scalar quantity and we do not have to consider the tensor S_{ij} .

132 An efficient way to evaluate the integrals in equations (1) or (2), is to invoke source-receiver reciprocity, turning
 133 both receiver locations into sources (Hanasoge, 2014; Xu et al., 2019). This is the approach taken in the ANSEICCA
 134 package, as detailed below. It is generally applicable because of assumption (i) listed above, which puts $P(\omega)$ outside
 135 the integral. Without this convenience, we note that Equation (3) below is not valid, and alternative computational
 136 techniques, such as the 'three-step' approach (see e.g. Tromp et al., 2010; Sager et al., 2018), need to be employed.

137 **2.1.1. Implementation**

138 ANSEICCA is purely a source inversion package and it works by assuming a fixed Earth structure model. Currently
 139 it is compatible with homogeneous acoustic, 1-D (depth dependent) elastic, and 2-D (laterally varying) acoustic media.
 140 The precise evaluation of equation (1) or (2) depends on the type of medium assumed:

- 141 1. Homogeneous acoustic medium – in this case the Green's function takes the analytic form $G(\mathbf{x}_A, \mathbf{x}; \omega) =$
 142 $H_0^{(1)}\left(\frac{\omega}{c}|\mathbf{x}_A - \mathbf{x}|\right)$, where $H_0^{(1)}$ is the Hankel function of the first kind of zeroth order, and c is the scalar
 143 wavespeed. This type of Green's function is internally calculated within the package (Datta et al., 2019).
- 144 2. 1-D elastic medium – here we use the surface wave terms of the elastodynamic Green's function, which are
 145 semi-analytically computable using surface wave theory in 1-D media (Malkoti et al., 2021; Datta, 2023). This
 146 type of Green's function is calculated by importing an external module from the package *SWID_earthsr*, which
 147 is a separate package available from AD's Github repository. This package is tied to the surface wave code
 148 'earthsr' (see Datta et al., 2017; Datta, 2018), which is based on the propagator matrix technique of Gomberg
 149 and Masters (1988).

3. 2-D acoustic medium – in this case we re-write equation (1) as

$$C(\mathbf{x}_A, \mathbf{x}_B) = \int d^2\mathbf{x} u^*(\mathbf{x}_A, \mathbf{x}) u(\mathbf{x}_B, \mathbf{x}) \sigma(\mathbf{x}), \quad (3)$$

150 with $u(\mathbf{x}_A, \mathbf{x}) = P(\omega)^{1/2} G(\mathbf{x}_A, \mathbf{x})$. Note that we have dropped the dependence on angular frequency ω , in the in-
 151 terest of a condensed notation. The wavefields u in equation (3) are obtained by numerically solving the acoustic
 152 wave equation with a source term equal to $P(\omega)^{1/2}$. This step of computing the wavefields is outsourced to the
 153 open-source Python package *Devito*, which implements finite difference modelling of seismic wave propagation
 154 (Louboutin et al., 2019; Luporini et al., 2020). Source-receiver reciprocity is invoked just as is done for equa-
 155 tions (1) and (2), implying that N numerical simulations are required in total, one per source at each of the N
 156 receivers (Datta et al., 2023).

In all three scenarios, once the appropriate Green's functions or wavefields are available, the cross-correlation for any pair of receivers is computed by approximating the spatial integrals of equations (1)-(3), as weighted sums over the modelling domain, similar to *noisi*. For example, equation 1 is implemented as:

$$C(\mathbf{x}_A, \mathbf{x}_B; \omega) \approx P(\omega) \sum_s [G^*(\mathbf{x}_s, \mathbf{x}_A; \omega) G(\mathbf{x}_s, \mathbf{x}_B; \omega) \sigma(\mathbf{x}_s)] (\Delta\mathbf{x})^2, \quad (4)$$

157 where the subscript s denotes individual grid points. This subscript is dropped from $\Delta\mathbf{x}$ because the grid is uniform.
 158 The errors introduced by the approximation represented in equation (4), have been analysed in detail by Ermert et al.
 159 (2020).

160 In this way, the ANSEICCA package separates the forward modelling into two steps — ‘primary forward mod-
 161 elling’, i.e. computation of Green's functions or wavefields, and the multiplication-summation required to evaluate the
 162 cross-correlation integral. This is in contrast to the aforementioned three-step approach, which does away with the
 163 need for multiplication and summation, but requires $2N$ numerical simulations (two simulations per receiver) in every
 164 iteration.

165 We note that ANSEICCA has been integrated with specifically chosen external packages, for the purpose of primary
 166 forward modelling in heterogeneous media. These packages may be replaced by others in the future, with minimal
 167 changes to the ANSEICCA code. All that is required is an interface module that takes the necessary parameters from
 168 ANSEICCA, and provides it the necessary Green's functions or wavefields. In this context, we also note that our
 169 package is currently not compatible with pre-computed databases of Green's functions or wavefields (e.g. *noisi* by
 170 Ermert et al., 2020). While this too can be implemented, we do not believe this will provide a major benefit because
 171 primary forward modelling is not a bottleneck of our code, for the reason discussed below.

172 2.1.2. Code optimization

173 In order to optimize the implementation described above, it is important to first note that primary forward modelling
 174 needs to be performed only once (it is done before the start of the iterative inversion – see Figure 4, Section 3), because
 175 the structure model is held fixed and hence G or u , do not change through the iterations. On the other hand, the cross-
 176 correlation integral needs to be evaluated afresh every iteration, because $\sigma(\mathbf{x})$ changes as the inversion proceeds. Hence
 177 from the point of view of optimization, it is important to focus on the integral evaluation. Equations (1)-(3) need to
 178 be applied to all pairs of receivers, which implies $N^2 C_2$ multiplication-summation operations, i.e. $O(N^2)$ operations,
 179 every iteration. This loop over receivers is a time-consuming exercise, which can be sped up by parallelization (see
 180 Section 3.3).

181 While the optimization of the primary modelling is less important, we have not ignored it.

- 182 1. Homogeneous and 1-D media: both these types of media are laterally homogeneous. We exploit the translational
 183 invariance of wave solutions in a laterally homogeneous medium, by primary forward modelling for a single
 184 source, rather than N sources. By choosing an ‘outer domain’ which is twice the size (four times the area) of the
 185 actual (square) modelling domain, it is possible to simulate the wavefield due to a source at any location within
 186 the actual domain. This is illustrated in Figure 1. In this way, the Green’s function due to a source at each of the
 187 N receivers, is obtained by modelling the solution due to a single source at the centre of a larger domain.
- 188 2. 2-D media: in this case, wavefields are computed using *Devito*, which generates highly optimized low-level C
 189 code for finite-difference solution of the acoustic wave equation.

190 2.2. Inversion

The aim of the inversion is to retrieve the source distribution $\sigma(\mathbf{x})$, using observations of cross-correlations $C(\mathbf{x}_A, \mathbf{x}_B)$
 for numerous receiver pairs $(\mathbf{x}_A, \mathbf{x}_B)$ within a receiver network. Unlike the forward theory described in Section 2.1,
 which is implemented with various modelling options, inverse modelling within the ANSEICCA package is rigidly
 implemented. It is predicated on matching the energies of observed and predicted cross-correlation waveforms. The
 misfit functional used to compare observed and predicted cross-correlations is (Hanasoge, 2013):

$$\chi = \frac{1}{2} \sum_i \left(\ln \frac{E_i^{\text{obs}}}{E_i^{\text{syn}}} \right)^2, \quad (5)$$

where the index i runs over all receiver pairs and E is the waveform energy in a time window $w(t)$:

$$E_{AB} = \sqrt{\int w(t) C_{AB}^2(t) dt}, \quad (6)$$

C_{AB} being shorthand for $\overline{C(\mathbf{x}_A, \mathbf{x}_B)}$. Inversion is driven by the so-called ‘source kernels’, which describe the sensitivity of cross-correlation energy to the source distribution $\sigma(\mathbf{x})$:

$$K_{AB}(\mathbf{x}) = \int d\omega f(\mathbf{x}_A, \mathbf{x}_B; \omega) G^*(\mathbf{x}_A, \mathbf{x}; \omega) G(\mathbf{x}_B, \mathbf{x}; \omega) P(\omega) \quad (7)$$

$$\text{OR } \int d\omega f(\mathbf{x}_A, \mathbf{x}_B; \omega) u^*(\mathbf{x}_A, \mathbf{x}; \omega) u(\mathbf{x}_B, \mathbf{x}; \omega). \quad (8)$$

The function f in equations (7)-(8) depends on the particular misfit used. Given the logarithmic misfit (5), Hanasoge (2013) obtained:

$$f(\mathbf{x}_A, \mathbf{x}_B; \omega) = \left(\frac{1}{E_{AB}^{syn}} \right)^2 C_{AB}^*(\omega) \quad (9)$$

191 The finite frequency kernels $K_{AB}(\mathbf{x})$ are continuous functions, but they are applied to a discrete inverse problem by
 192 parameterizing the model space in terms of a finite set of basis functions (see equation (12) in the Appendix). The
 193 inverse problem therefore reduces to a problem of estimating the basis function coefficients, which can be solved by
 194 any of the standard optimization techniques of discrete inverse theory. We use the Gauss-Newton method, as detailed
 195 in Section (Appendix) 8. Note that optimization is not directly applied to the quantity of interest, $\sigma(\mathbf{x})$, but to the basis
 196 function coefficients, m_j . The former must be obtained from the latter using equation (12).

197 2.2.1. Implementation

198 The ANSEICCA package contains a raw implementation of the inversion scheme detailed in Section (Appendix)
 199 8. Similar to forward modelling, the inversion process can be seen as separated into two parts — calculation of
 200 measurements and kernels, which is done within the package’s core module (*h13*, see Table 3), and optimization using
 201 the Gauss-Newton algorithm, which is handled by one of the utility modules (*u1*, see Table 3). The code is structured
 202 such that both parts are integrated into an explicit *while* loop, which runs until the inversion converges or hits a cap
 203 on the number of iterations. This structure is facilitated by the fact that the optimization does not rely on any in-built
 204 Python routines, such as from the SciPy `minimize` module¹. Instead, after computing the gradient and approximate
 205 Hessian in any iteration, equation (20) is explicitly solved (using NumPy’s *linalg* module) to obtain the model update.
 206 The entire inverse modelling workflow, from measurements to optimization, is implemented separately for positive
 207 and negative-branch measurements, and the results averaged at the end of an iteration, to update the model.

208 Inversion is deemed to have converged when the data misfit ceases to change (decrease) by more than a threshold
 209 value (e.g. 2 or 5%), which is hardwired into the code. Synthetic tests reveal that this typically happens in a relatively

¹we have tried the L-BFGS and conjugate-gradient algorithms from `scipy.minimize`. Use of this module requires non-trivial modification of the code (no explicit loop over iterations) and does not produce improved results, therefore we have not retained this option in the code.

Module	Shorthand
In <i>anseicca</i> :	
<i>hans2013_serial.py</i> or <i>hans2013_parallel.py</i>	h13
In <i>modules_common</i> :	
<i>cctomo_utis1.py</i>	u1
<i>cctomo_utis2.py</i>	u2
<i>utis_io.py</i>	uio
<i>validate_params.py</i>	val

Table 1

Code modules and corresponding short names used in this paper.

210 small number of iterations, on the order of 10. Figure 2 shows the progress of inversion in the ‘E1’ example provided
211 with the package.

212 2.2.2. Code optimization

213 The bottleneck in the inversion workflow described above, is the calculation of pairwise source kernels. This
214 calculation is parallelized in the same way as the evaluation of cross-correlation integrals for forward modelling (see
215 Section 3.3).

216 3. Detailed code description

217 The source code of the ANSEICCA package comprises two directories: *anseicca* and *modules_common*. Two
218 types of code are contained within *anseicca*: serial and parallel. Each comes with its own ‘wrapper’ program (*an-*
219 *seicca_wrapper_serial* or *anseicca_wrapper_parallel*) and core module (*hans2013_serial* or *hans2013_parallel*), but
220 all other modules are common to the serial and parallel codes. These modules are also shared with a related but sep-
221 arate package of code, currently under development, which is meant for structure inversion. Hence these modules are
222 bundled together in the appropriately-named *modules_common* directory.

223 Figure 3 shows the overall code structure. It should serve as a handy reference for the detailed code description
224 below.

225 3.1. Running the code

226 To run the serial or parallel code, one simply needs to run the corresponding wrapper (specifying the correct
227 number of processors in the parallel case, see Section 3.3). Two controls are provided in the wrapper programs, via
228 the following boolean flags:

- 229 1. *do_inv*: if *True*, the code executes to completion – as determined by the second flag described below – and
230 produces an output file (see Section 3.2.2). If set to *False*, the code executes only up to the ‘set up’ stage; no
231 forward or inverse modelling is performed, and no output file produced. The *False* setting is useful for plotting

232 and visualization purposes.

233 2. *iter_only1*: if *False*, inversion proceeds until ‘natural’ termination as per the criteria laid out in Section 2.2. If
 234 set to *True*, the inversion is force-terminated after one iteration. The *True* setting is useful for testing and forward
 235 modelling purposes.

236 All other code settings, including parameter specifications, are provided in a parameter file called *Par_file*, which is
 237 described in detail in the code manual. Beginners or novice programmers need only interface with the wrapper and
 238 the *Par_file*, to use the code as is.

239 3.2. I/O

240 All of the code’s I/O operations are handled by the *utils_io* module.

241 3.2.1. Input

242 The minimum input for the package consists of two files with hardwired names and locations:

- 243 (i) *receivers.csv* – a text file containing the list of stations or receivers with their IDs and location coordinates (see
 244 manual for format).
- 245 (ii) *Par_file* – a text file specifying the values of various simulation parameters (see manual for detailed description).

246 This file must be compatible with *modules_common/config.py*, which reads it using Python’s *configparser* utility.

247 Both these files need to be present in the *INPUT* sub-directory within *anseicca*. We distinguish between this ‘primary
 248 input’, which is always required regardless of use case, and additional ‘secondary input’ which may be required de-
 249 pending on the type of usage. Secondary input is provided interactively, via code prompts generated in accordance
 250 with the relevant *Par_file* settings. The following quantities constitute possible secondary input:

- 251 (a) Data to be inverted – a single directory containing observed interstation cross-correlations. This input is required
 252 whenever the package is used to invert pre-existing data stored on disk, such as any real data set (*Par_file* setting:
 253 *ext_data = True*). Details of compatible data formats are provided in the code manual. Note that the code can
 254 handle ‘missing data’, so the cross-correlations available in the data directory, may correspond to any subset of all
 255 possible station pairs. The recommended location for this directory is *anseicca/INPUT/DATA*.
- 256 (b) 1-D elastic model(s) – a single directory containing an elastic Earth model file, plus the associated dispersion
 257 and eigenfunction files compatible with the *SWID_earthsr* package (Section 2.1.1?). This input is required when
 258 analytical, elastic modelling is chosen for inversion and/or for the generation of test data (in *Par_file* settings).
- 259 (c) 2-D velocity model(s) – a single file to be used either for inversion, or for the generation of test data (two separate
 260 files may be provided for the two purposes). This input is required when numerical, acoustic modelling is chosen

261 for inversion and/or test data generation (in *Par_file* settings). The velocity model files must be in *.npz* format,
 262 compatible with *modules_common/read_velocity_models.py*.

263 (d) Receiver list – a single file specifying the receiver IDs to be included in the simulation, with a single receiver per
 264 line. This input is solicited (not required) whenever the number of receivers in the *Par_file* is set to less than the
 265 total number of receivers contained in *receivers.csv*. If no input is provided, the desired number of receivers is
 266 selected automatically using an internal criterion (which penalises receiver location error arising from mapping
 267 actual receiver coordinates, onto a uniform grid).

268 With reference to points (a)-(c) in the list above, we note that it is possible to run synthetic test inversions (e.g.
 269 Datta et al., 2023) without pre-existing data. As a legacy from its humble origins in the MATLAB code of Hanasoge
 270 (2013), the *anseicca* package is designed to include an ‘internal data’ mode. In this mode of operation (*Par_file*
 271 setting: *ext_data = False*), synthetic data is generated internally for a chosen ‘true model’, stored in memory, and then
 272 inverted — all in a single code run. In order to avoid the ‘inverse crime’ of computing and inverting ‘data’ using the
 273 same modelling scheme, one only needs to specify different modelling parameters for the generation of test data, and
 274 for inversion. The *Par_file* and the secondary input are designed to specify these two sets of parameters completely
 275 independently. For example, Datta et al. (2019) had demonstrated the use of different model parameterizations for the
 276 test data and inversion. Datta et al. (2023) additionally showed how, with acoustic modelling, different velocity models
 277 can be used in the two cases.

278 We use the terms ‘internal data’ and ‘external data’ for data generated internally, and data read from disk, respec-
 279 tively. Internal data is always synthetic, whereas external data may be real or synthetic.

280 3.2.2. Output

281 The output of the code, regardless of whether serial or parallel, consists of a single *.pckl* file produced using Python’s
 282 *pickle* module. In addition to the results (both final and intermediate) of a code run, the output file contains all the
 283 necessary settings and parameter values required to reproduce the run. This can save users a lot of tedious bookkeeping,
 284 as simulation parameters do not need to be recorded or documented separately.

285 The *view_output_anseicca.py* script, in the *anseicca* directory, can be used to visualize the output. It relies on
 286 *read_pickled_output.py*, from *modules_common*, to de-serialize the input, and provides a host of options for plotting
 287 various quantities. The code manual provides a comprehensive demonstration of all plotting options, several of which
 288 have been used to produce figures shown in this paper as well as previous related ones.

289 Finally, *view_output_anseicca.py* also allows the user to save the (synthetic) cross-correlation waveforms generated
 290 during a code run and contained in the output file, as individual SAC files. This can be used to create a directory of
 291 ‘data’, which can serve as input to the code in a future run.

292 3.3. Parallelization

293 As depicted in Figure 3, only the core module of this package, *hl3*, is parallelized. All other processes in the overall
 294 code flow, are executed exclusively on the master processor (rank = 0). Within the core module, the computationally
 295 expensive processes are cross-correlation modelling, and the calculation of pairwise source kernels (see Figure 4).
 296 Both of these require multiplication and summation operations to be performed for every pair of receivers. This implies
 297 $O(N^2)$ calculations, for N receivers. In the serial code, these processes are each implemented via a nested for-loop
 298 structure. On the other hand, the parallel code distributes the pairwise calculations across processors, reducing the
 299 number of operations from $O(N^2)$ to $O(N)$, per processor. Therefore the speed-up achieved by parallelization, scales
 300 with N .

301 It works by setting the number of processors to be equal to the number of receivers. The i^{th} processor is assigned
 302 the task of performing the calculations for all receiver pairs (j, i) , where $i < j \leq N$. Thus the i^{th} processor handles
 303 $N - i$ receiver pairs, implying that the first processor performs the most calculations, and the last processor performs
 304 none.

305 In the calculation of source kernels, we note that results from individual processors need to be combined to build
 306 the complete \mathbf{G} (Jacobian) matrix, because each processor can contribute only some part (rows) of this matrix, through
 307 equation (16).

308 Finally, we wish to point out that the parallelization described here refers only to code operations performed within
 309 the ANSEICCA package. In the rigorous use case of 2-D acoustic modelling, the primary forward modelling (out-
 310 sourced to Devito) may itself be computationally demanding, but is currently not parallelized. However this is not a
 311 major bottleneck because of reasons noted earlier:

- 312 (a) the number of numerical simulations required is N , not $O(N^2)$
- 313 (b) these simulations need to be performed only once, not repeated every iteration.

314 3.4. Working with real data

315 Inversion of real data involves a few important considerations and code operations, which are exclusive to the
 316 external data usage mode. These details are hidden in the flowcharts of Figures 3 and 4, so we highlight them in this
 317 section. The *u2* module has been devoted to these specific operations, as detailed below:

- 318 1. Estimation of signal-to-noise ratio (SNR) – this is part of the ‘read and process data’ step in Figure 3. The *u2*
 319 module’s *cc_data* class, which reads the data, includes a *Process* sub-class which calculates the SNR of the
 320 individual cross-correlation waveforms. The SNR values are converted to data errors, which constitute the data
 321 covariance matrix used in inversion (see Section 2.2). Conversion of SNR to error values is subject to user
 322 discretion (e.g. Datta et al., 2019), but must be hardwired into the *u2* module.

- 323 2. Choice of measurement window – the time window $w(t)$ used to define the data measurement is taken to be the
 324 same as that used to calculate SNR values. Hence the choice of $w(t)$ is also hardwired into the u2 module.
- 325 3. Estimation of $P(\omega)$ – this is done in two stages. First, as part of the ‘read and process data’ step in Figure 3, the
 326 shape of $P(\omega)$ is determined by averaging the power spectra of all the cross-correlation waveforms in the data set
 327 (done by the *source_spectrum* class in module u2). In the second stage, its amplitude is adjusted in the ‘estimate
 328 average initial amplitudes’ step of Figure 4, i.e. in the first iteration of the nonlinear inversion undertaken by the
 329 h13 module. The criterion used for fixing the amplitude of $P(\omega)$, is that the energies of the initially predicted
 330 data should match those of the observed data, in some average sense. We choose to fit the decay of observed
 331 energies as a function of distance (see Figure 5).

332 3.5. Detailing of individual code files

333 3.5.1. Core ANSEICCA programs or modules: the *anseicca* directory

- 334 • *anseicca_wrapper_serial* or *anseicca_wrapper_parallel*: wrapper for the serial or parallel versions of the code,
 335 respectively.
- 336 • *hans2013_serial* and *hans2013_parallel*: serial and parallel versions respectively, of the ‘core’ code module.
- 337 • *view_output_anseicca*: module used for visualization of code output; requires a pickle file, or directory contain-
 338 ing pickle files, as input.

339 3.5.2. Utility modules: the *modules_common* directory

- 340 • *config*: configuration module containing definitions of globally used functions and user-defined data structures;
 341 assigns values to various simulation parameters by reading the *Par_file* using Python’s *configparser* utility.
- 342 • *cctomo_utils1*: contains the mandatorily required code utilities, i.e. those which are independent of whether
 343 the data is internal or external — set up of the modeling domain, adding Gaussian noise to synthetic cross-
 344 correlations, all types of source (model) parameterizations, inversion.
- 345 • *cctomo_utils2*: contains those code utilities which are relevant only in case of external data (see section RD
 346 above) — fitting of $1/r$ curve to cross-correlation energy as a function of distance, estimation of the source
 347 power spectrum $P(\omega)$, reading and processing of data, calculation/assignment of data errors.
- 348 • *read_pickle_output*: reads the code output, i.e. the pickle file produced by *utils_io*; also does the groundwork
 349 for some of the operations of *view_output_anseicca*.
- 350 • *utils_io*: handles all input/output operations. For input, it reads the stations file and velocity/structure model
 351 files. The input models are currently limited to 1-D (depth-dependent) elastic and 2-D (x-y?) acoustic models.

		Compute time (s)					
		10		20		50	
Grid size	Number of receivers	Serial	Parallel	Serial	Parallel	Serial	Parallel
		51 × 51		5	6	15	13
101 × 101		19	11	69	16	432	75
201 × 201		68	34	285	99	1958	374

Table 2

Computing time to complete one iteration of inversion, for various model sizes and receiver array densities.

- 352 • *utils_plotting*: contains various plotting utilities.
- 353 • *validate_params*: performs basic checks on parameter values (for aliasing, memory requirement etc.), before
354 the core code is allowed to run.

355 4. Benchmarking

356 We provide some performance benchmarks using variations of the ‘E1’ example provided along with the package,
357 which corresponds to the test model shown in Figure 2(a). The canonical setup for this example entails 20 receivers, a
358 center frequency of 0.2 Hz and a model size of 101×101 grid points (see Datta et al., 2023). Here we perform inversions
359 using essentially the same setup, but with three different model sizes and either 10, 20 or 50 receivers (Figure 6). Note
360 that ‘model size’ here refers to the number of grid points, not the number of model parameters, which is the same in all
361 tests (625, see Datta et al., 2023). These benchmark tests are run on an HPC system with 2.9 GHz Intel Xeon Platinum
362 8268 processors, and 48 processors per node.

363 For each test, the time required to complete one iteration of inversion, is listed in Table 4. These times include the
364 time taken to generate the test data, because the code is run in internal data mode. Note how the difference between
365 the serial and parallel compute times, scales with the number of receivers. For reference, a complete inversion in the
366 most compute-heavy scenario, 201 × 201 grid and 50 receivers, took just over an hour (3800 s), with 15 iterations.

367 We wish to point out that the same tests run significantly faster on an iMac with a 3.6 GHz Intel Core i9 processor,
368 and 64 GB RAM. For example with 50 receivers, the serial code on the iMac yields single-iteration run times of 57,
369 261 and 1070 s, for the three model sizes considered. Yet faster run times are achieved on an iMac with an Apple M1
370 chip. We are unable to run the parallel code on the iMacs, due to the small number of processors available (< 10).

371 5. Discussion and Conclusion

372 We have presented a useful computational seismology package, ANSEICCA, for seismic ambient noise cross-
373 correlation modelling and noise source inversion, at local scales. It is written in Python and has been parallelised for
374 efficiency. At a deeper level, it utilizes optimized C code for seismic wave propagation modelling in heterogeneous

375 media, but this too is facilitated by a Python package (Devito), so the convenience of the Python environment is
376 maintained throughout.

377 ANSEICCA is extremely ‘lightweight’ – it has no storage requirements and its memory requirements, on the order
378 of one to tens of GB depending on grid size, are easily met by modern computers. It is also highly modular, which makes
379 it easily extensible. For example, it currently leverages Devito for 2-D acoustic modelling. This can be augmented
380 to 3-D elastic modelling in future, simply by writing a new module to interface with Devito. Taking this idea a step
381 further, ANSEICCA could also be linked to other wave propagation solvers in future, should the need arise to go
382 beyond Devito.

383 The drawbacks of ANSEICCA, from an implementation perspective, are its rigid cartesian grid (which cannot
384 account for Earth’s sphericity or surface topography), and the approximation of integrals with weighted sums. Apart
385 from this, there currently exist two conceptual limitations — the assumption of a uniform noise source spectrum, and
386 the inability to account for the Earth’s three-dimensional elastic (or anelastic) structure.

387 With these limitations in mind, we intend to continuously maintain and further develop the ANSEICCA package.
388 This paper makes ANSEICCA accessible for immediate use as well as development by other interested researchers in
389 the community.

390 **6. Acknowledgements**

391 AD thanks Shravan Hanasoge for providing the seed MATLAB code in 2018, for the calculation of source kernels,
392 which lie at the heart of this package. We thank Bharath Shekar for introducing us to Devito, and writing the interface
393 module between ANSEICCA and Devito. AM gratefully acknowledges financial support from the INSPIRE Fellow-
394 ship [IF200455], Department of Science & Technology, Government of India. The support and resources provided by
395 the Param Brahma HPC facility under the National Supercomputing Mission, Government of India, at IISER Pune are
396 gratefully acknowledged.

397 **7. Code availability**

398 The ANSEICCA package is available at https://github.com/arjundatta23/cc_kern_inv. Supporting code
399 is available at https://github.com/arjundatta23/SW1D_earthsr (for *SW1D_earthsr*) and
400 <https://github.com/devitocodes/devito> (for *Devito*).

401 **References**

402 Bowden, D.C., Tsai, V.C., Lin, F.C., 2015. Site amplification, attenuation, and scattering from noise correlation amplitudes across a dense array in
403 long beach, ca. Geophysical Research Letters doi:10.1002/2014GL062662.

- 404 Dalcín, L., Paz, R., Storti, M., 2005. MPI for Python. *J. Parallel Distrib. Comput.* 65, 1108 – 1115. doi:10.1016/j.jpdc.2005.03.010.
- 405 Datta, A., 2018. Swrt: A package for semi-analytical solutions of surface wave propagation, including mode conversion, across trans-
406 versely aligned vertical discontinuities. *Geoscientific Instrumentation, Methods and Data Systems* 7, 101–112. URL: [https://www.](https://www.geosci-instrum-method-data-syst.net/7/101/2018/)
407 [geosci-instrum-method-data-syst.net/7/101/2018/](https://www.geosci-instrum-method-data-syst.net/7/101/2018/), doi:10.5194/gi-7-101-2018.
- 408 Datta, A., 2023. Reply to comment on Malkoti et al. (2021) by Haney and Nakahara. *Geophysical Journal International* 234, 1965–1969. URL:
409 <https://academic.oup.com/gji/article/234/3/1965/7146201>, doi:10.1093/GJI/GGAD179.
- 410 Datta, A., Hanasoge, S., Goudswaard, J., 2019. Finite frequency inversion of cross-correlation amplitudes for ambient noise source directivity
411 estimation. *Journal of Geophysical Research: Solid Earth* 124, 6653–6665. URL: [https://onlinelibrary.wiley.com/doi/abs/10.](https://onlinelibrary.wiley.com/doi/abs/10.1029/2019JB017602)
412 [1029/2019JB017602](https://onlinelibrary.wiley.com/doi/abs/10.1029/2019JB017602), doi:10.1029/2019JB017602.
- 413 Datta, A., Priestley, K.F., Roecker, S., Chapman, C.H., 2017. Surface wave mode coupling and the validity of the path average approximations in
414 surface waveform inversions: an empirical assessment. *Geophys. J. Int.* 211, 1099–1120.
- 415 Datta, A., Shekar, B., Kumar, P.L., 2023. Acoustic full waveform inversion for 2-d ambient noise source imaging. *Geophysical Journal International*
416 234, 1628–1639. URL: <https://academic.oup.com/gji/article/234/3/1628/7117958>, doi:10.1093/GJI/GGAD158.
- 417 Denolle, M.A., Dunham, E.M., Prieto, G.A., Beroza, G.C., 2013. Ground motion prediction of realistic earthquake sources using the ambient
418 seismic field. *Journal of Geophysical Research: Solid Earth* 118, 2102–2118. doi:10.1029/2012JB009603.
- 419 Ermert, L., Igel, J., Sager, K., Stutzmann, E., Nissen-Meyer, T., Fichtner, A., 2020. Introducing noisi: A python tool for ambient noise cross-
420 correlation modeling and noise source inversion. *Solid Earth* 11, 1597–1615. doi:10.5194/SE-11-1597-2020.
- 421 Fichtner, A., 2014. Source and processing effects on noise correlations. *Geophysical Journal International* 197, 1527–1531. URL: [http://](http://academic.oup.com/gji/article/197/3/1527/657661/Source-and-processing-effects-on-noise)
422 academic.oup.com/gji/article/197/3/1527/657661/Source-and-processing-effects-on-noise, doi:10.1093/gji/ggu093.
- 423 Fichtner, A., Stehly, L., Ermert, L., Boehm, C., 2017. Generalized interferometry – i: theory for interstation correlations. *Geophysical Journal*
424 *International* 208, 603–638. URL: <https://academic.oup.com/gji/article-lookup/doi/10.1093/gji/ggw420>, doi:10.1093/gji/
425 [ggw420](https://academic.oup.com/gji/article-lookup/doi/10.1093/gji/ggw420).
- 426 Fichtner, A., Tsai, V.C., 2019. Theoretical Foundations of Noise Interferometry, in: Nakata, N., Gualtieri, L., Fichtner, A. (Eds.), *Seismic*
427 *Ambient Noise*. 1 ed.. Cambridge University Press, pp. 109–143. URL: [https://www.cambridge.org/core/product/identifier/](https://www.cambridge.org/core/product/identifier/9781108264808%23c4/type/book_part)
428 [9781108264808%23c4/type/book_part](https://www.cambridge.org/core/product/identifier/9781108264808%23c4/type/book_part), doi:10.1017/9781108264808.006.
- 429 Gomberg, J.S., Masters, T.G., 1988. Waveform modelling using locked-mode synthetic and differential seismograms: application to determination
430 of the structure of Mexico. *Geophysical Journal* 94, 193–218. doi:10.1111/j.1365-246X.1988.tb05896.x.
- 431 Halliday, D., Curtis, A., 2008. Seismic interferometry, surface waves and source distribution. *Geophysical Journal International* 175,
432 1067–1087. URL: <https://academic.oup.com/gji/article-lookup/doi/10.1111/j.1365-246X.2008.03918.x>, doi:10.1111/
433 [j.1365-246X.2008.03918.x](https://academic.oup.com/gji/article-lookup/doi/10.1111/j.1365-246X.2008.03918.x).
- 434 Hanasoge, S.M., 2013. The influence of noise sources on cross-correlation amplitudes. *Geophysical Journal International* 192, 295–309. URL:
435 <http://academic.oup.com/gji/article/192/1/295/594723/The-influence-of-noise-sources-on-crosscorrelation>,
436 doi:10.1093/gji/ggs015.
- 437 Hanasoge, S.M., 2014. Measurements and kernels for source-structure inversions in noise tomography. *Geophysical Journal International* 196,
438 971–985. doi:10.1093/gji/ggt411.
- 439 Igel, J.K., Ermert, L.A., Fichtner, A., 2021. Rapid finite-frequency microseismic noise source inversion at regional to global scales. *Geophysical Jour-*
440 *nal International* 227, 169–183. URL: <https://academic.oup.com/gji/article/227/1/169/6287575>, doi:10.1093/GJI/GGAB210.
- 441 Kimman, W.P., Trampert, J., 2010. Approximations in seismic interferometry and their effects on surface waves. *Geophysical Journal International*

- 442 182, 461–476. URL: <https://academic.oup.com/gji/article-lookup/doi/10.1111/j.1365-246X.2010.04632.x>, doi:10.1111/
 443 j.1365-246X.2010.04632.x.
- 444 Lobkis, O.I., Weaver, R.L., 2001. On the emergence of the green's function in the correlations of a diffuse field. *The Journal of the Acoustical*
 445 *Society of America* 110, 3011–3017. URL: <http://asa.scitation.org/doi/10.1121/1.1417528>, doi:10.1121/1.1417528.
- 446 Louboutin, M., Lange, M., Luporini, F., Kukreja, N., Witte, P.A., Herrmann, F.J., Velesko, P., Gorman, G.J., 2019. Devito (v3.1.0): an embedded
 447 domain-specific language for finite differences and geophysical exploration. *Geoscientific Model Development* 12, 1165–1187. URL: <https://www.geosci-model-dev.net/12/1165/2019/>, doi:10.5194/gmd-12-1165-2019.
- 448
- 449 Luporini, F., Louboutin, M., Lange, M., Kukreja, N., Witte, P., Hückelheim, J., Yount, C., Kelly, P.H.J., Herrmann, F.J., Gorman, G.J., 2020.
 450 Architecture and performance of devito, a system for automated stencil computation. *ACM Trans. Math. Softw.* 46. URL: [https://doi.org/](https://doi.org/10.1145/3374916)
 451 [10.1145/3374916](https://doi.org/10.1145/3374916), doi:10.1145/3374916.
- 452 Malkoti, A., Datta, A., Hanasoge, S.M., 2021. Rayleigh-wave h/v ratio measurement from ambient noise cross-correlations and its sensitivity to
 453 vp: a numerical study. *Geophysical Journal International* 227, 472–482. URL: [https://academic.oup.com/gji/article/227/1/472/](https://academic.oup.com/gji/article/227/1/472/6296642)
 454 [6296642](https://academic.oup.com/gji/article/227/1/472/6296642), doi:10.1093/GJI/GGAB228.
- 455 Menke, W., 2012. *Geophysical Data Analysis: Discrete Inverse Theory*. Academic Press.
- 456 Roten, D., Fäh, D., Cornou, C., Giardini, D., 2006. Two-dimensional resonances in alpine valleys identified from ambient vibration wavefields.
 457 *Geophysical Journal International* 165, 889–905. doi:10.1111/J.1365-246X.2006.02935.X/3/165-3-889-FIG031.JPEG.
- 458 Sager, K., Boehm, C., Ermert, L., Krischer, L., Fichtner, A., 2020. Global-scale full-waveform ambient noise inversion. *Journal of Geophysical*
 459 *Research: Solid Earth* 125, e2019JB018644. doi:10.1029/2019jb018644.
- 460 Sager, K., Ermert, L., Boehm, C., Fichtner, A., 2018. Towards full waveform ambient noise inversion. *Geophysical Journal International* 212,
 461 566–590. URL: <http://academic.oup.com/gji/article/212/1/566/4411809>, doi:10.1093/gji/ggx429.
- 462 Shapiro, N.M., Campillo, M., 2004. Emergence of broadband rayleigh waves from correlations of the ambient seismic noise. *Geophysical Research*
 463 *Letters* 31, n/a–n/a. URL: <http://doi.wiley.com/10.1029/2004GL019491>, doi:10.1029/2004GL019491.
- 464 Stehly, L., Boué, P., 2017. On the interpretation of the amplitude decay of noise correlations computed along a line of receivers. *Geophysical Journal*
 465 *International* 209, 358–372. URL: <https://academic.oup.com/gji/article-lookup/doi/10.1093/gji/ggx021>, doi:10.1093/gji/
 466 [ggx021](https://academic.oup.com/gji/article-lookup/doi/10.1093/gji/ggx021).
- 467 Tarantola, A., 2005. *Inverse Problem Theory and Methods for Model Parameter Estimation*. Society for Industrial and Applied Mathematics.
 468 doi:10.1137/1.9780898717921.
- 469 Tromp, J., Luo, Y., Hanasoge, S., Peter, D., 2010. Noise cross-correlation sensitivity kernels. *Geophysical Journal International* 183,
 470 791–819. URL: <https://academic.oup.com/gji/article-lookup/doi/10.1111/j.1365-246X.2010.04721.x>, doi:10.1111/j.
 471 [1365-246X.2010.04721.x](https://academic.oup.com/gji/article-lookup/doi/10.1111/j.1365-246X.2010.04721.x).
- 472 Xu, Z., Mikesell, T.D., Gribler, G., Mordret, A., 2019. Rayleigh-wave multicomponent cross-correlation-based source strength distribution inver-
 473 sion. part 1: Theory and numerical examples. *Geophysical Journal International* 218, 1761–1780. URL: [https://academic.oup.com/gji/](https://academic.oup.com/gji/article/218/3/1761/5510447)
 474 [article/218/3/1761/5510447](https://academic.oup.com/gji/article/218/3/1761/5510447), doi:10.1093/gji/ggz261.
- 475 Yao, H., van der Hilst, R.D., 2009. Analysis of ambient noise energy distribution and phase velocity bias in ambient noise tomography, with
 476 application to se tibet. *Geophysical Journal International* 179, 1113–1132. URL: [https://academic.oup.com/gji/article-lookup/](https://academic.oup.com/gji/article-lookup/doi/10.1111/j.1365-246X.2009.04329.x)
 477 [doi/10.1111/j.1365-246X.2009.04329.x](https://academic.oup.com/gji/article-lookup/doi/10.1111/j.1365-246X.2009.04329.x), doi:10.1111/j.1365-246X.2009.04329.x.

478 8. APPENDIX 1: Inversion algorithm

Equation (5) can be written as

$$\chi = \frac{1}{2} \sum_i \Delta d_i^2, \quad (10)$$

479 where $\Delta d_i = \ln E_i^{\text{obs}} - \ln E_i^{\text{syn}}$.

Variations in the misfit are related to variations in the model parameters (spatial source distribution $\sigma(\mathbf{x})$) via the misfit kernel $K(\mathbf{x})$:

$$\delta\chi = - \int K(\mathbf{x}) \delta\sigma(\mathbf{x}) d^2\mathbf{x} \quad (11)$$

Since the model space is parameterized using a set of 2-D Gaussian basis functions (Datta et al., 2023):

$$\sigma(\mathbf{x}) = \sum_j m_j^2 B_j(\mathbf{x}), \quad (12)$$

the model perturbation can be expanded into the model space basis functions, $B_j(\mathbf{x})$:

$$\delta\sigma(\mathbf{x}) = \sum_{j=1}^M 2m_j \delta m_j B_j(\mathbf{x}) \quad (13)$$

Also, the misfit kernel is the sum of individual source kernels for each receiver pair, weighted by the corresponding data misfit:

$$K = \sum_i \Delta d_i K_i(\mathbf{x}) = \sum_i \ln \left(\frac{E_i^{\text{obs}}}{E_i^{\text{syn}}} \right) K_i(\mathbf{x}) \quad (14)$$

As shown in Datta et al. (2019, 2023), equations (11), (13) and (14) produce the gradient \mathbf{g} of χ , as well as the Jacobian matrix (\mathbf{G}) which linearizes the inverse problem:

$$g_j = \frac{\partial\chi}{\partial m_j} = - \int 2K(\mathbf{x}) m_j B_j(\mathbf{x}) d^2\mathbf{x} = -G_{ij} \Delta d_i, \quad (15)$$

where

$$G_{ij} = \int 2K_i(\mathbf{x}) m_j B_j(\mathbf{x}) d^2\mathbf{x}. \quad (16)$$

In matrix notation, we have

$$\mathbf{g} = -\mathbf{G}^T \Delta \mathbf{d} \quad (17)$$

Similarly, the Jacobian matrix yields the approximate Hessian for a Gauss-Newton inversion:

$$\mathbf{H} = \mathbf{G}^T \mathbf{G} \quad (18)$$

In practice, equations (17) and (18) are modified to incorporate weighting and damping (see e.g. Menke, 2012):

$$\begin{aligned} \tilde{\mathbf{g}} &= -\mathbf{G}^T \mathbf{C}_D^{-1} \Delta \mathbf{d} - \mathbf{C}_M^{-1} (\mathbf{m} - \mathbf{m}_0) \\ \tilde{\mathbf{H}} &= \mathbf{G}^T \mathbf{C}_D^{-1} \mathbf{G} + \mathbf{C}_M^{-1} \end{aligned} \quad (19)$$

where \mathbf{C}_D and \mathbf{C}_M are the data and model covariance matrices, respectively, and \mathbf{m}_0 is a prior model about which the inversion is damped (also serving as the starting model for iterative inversion). The form of damping represented by equation (19) requires that the the model vector comprises the basis function coefficients, m_j . Hence it is these coefficients that are directly updated by iterative optimization. The Gauss-Newton method (Menke, 2012; Tarantola, 2005) yields:

$$[\mathbf{G}_k^T \mathbf{C}_D^{-1} \mathbf{G}_k + \mathbf{C}_M^{-1}] \Delta \mathbf{m}_k = [\mathbf{G}_k^T \mathbf{C}_D^{-1} \Delta \mathbf{d}_k + \mathbf{C}_M^{-1} (\mathbf{m}_k - \mathbf{m}_0)] \quad (20)$$

or

$$\mathbf{m}_{k+1} = \mathbf{m}_k + [\mathbf{G}_k^T \mathbf{C}_D^{-1} \mathbf{G}_k + \mathbf{C}_M^{-1}]^{-1} [\mathbf{G}_k^T \mathbf{C}_D^{-1} \Delta \mathbf{d}_k + \mathbf{C}_M^{-1} (\mathbf{m}_k - \mathbf{m}_0)] \quad (21)$$

480 **List of Figures**

481 1 ‘Outer domain’ source trick used for laterally homogeneous media, illustrated using the modelling
 482 geometry of Malkoti et al. (2021). Here the actual modelling domain is of size 1200×1200 km,
 483 shown by the inner square with solid lines. The desired quantity is the Green’s function throughout
 484 this domain, due to a source at the receiver location marked by the inverted triangle. In the ANSEICCA
 485 implementation, an outer domain of size 2400×2400 km is used and the Green’s function calculated
 486 throughout it, for a source at the origin (red dot). The obtained solution is shown here in colour,
 487 at some arbitrary frequency. The desired quantity is then obtained by simply windowing this outer
 488 domain solution, using the square marked with dashed lines. This square is the same size as the actual
 489 domain, but is centred (open white circle) at the mirror image, with respect to the origin, of the actual
 490 receiver location. Thus by positioning the window appropriately, the solution can be obtained for a
 491 source at any location within the modelling domain. 20

492 2 Synthetic test to illustrate inversion progress. (a) The test model for the E1 example; note that this is
 493 the same model as in Figure 2d of Datta et al. (2023). (b) Evolution of the model with progress of
 494 inversion (as indicated by the iteration number k in each panel); note the homogeneous starting model
 495 in the top left, and the inversion result in the bottom right. (c) Evolution of data misfit, showing $\approx 99\%$
 496 misfit reduction in this synthetic example. 21

497 3 Flowchart of the overall structure of the package, essentially mirroring the wrapper programs. The highlighted
 498 (yellow) process in this flowchart is the one that is parallelised (see Section 3.3). The dashed circular inputs
 499 associated with any step or process represent the modules used for its implementation, as per the nomenclature
 500 of Table 3. We note that the *config* module is not shown here, but is used ubiquitously. See Section 3.2.1 for the
 501 definitions of ‘internal/external’ data. 22

502 4 Flowchart showing the detailed structure of the core module, h13. The two highlighted boxes, which are part of
 503 the inversion loop, represent code operations that are parallelized. Other symbols have the same meaning as in
 504 Figure 3. 23

505 5 Example of curve-fitting for observed cross-correlation energy as a function of inter-receiver distance r , taken
 506 from the test data of example E1. The blue circles show the observed energies, and the black line is the best fitting
 507 $1/r$ curve. Energies are normalised with respect to the maximum observed value. First-iteration synthetics in an
 508 inversion will be scaled such that their energies match the black curve. 24

509 6 Inversion setup and results related to the benchmark tests. (a)-(c) Receiver maps showing the selection
 510 of 10, 20 and 50 receivers (dark red triangles), along with inter-receiver paths (grey lines). (d)-(f)
 511 Corresponding inversion results (after completion of all iterations) for a model size of 101×101 . Note
 512 that (b), (e) correspond to Figure 2. 25

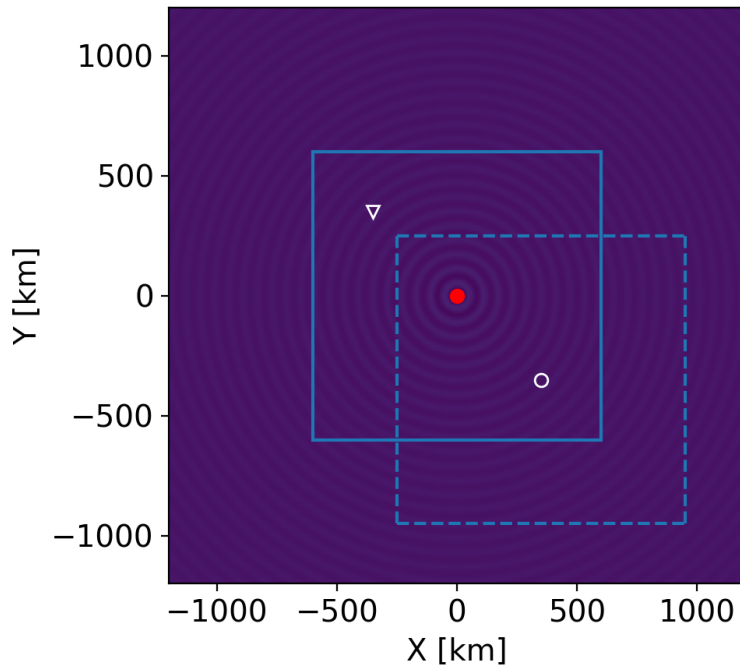


Figure 1: ‘Outer domain’ source trick used for laterally homogeneous media, illustrated using the modelling geometry of Malkoti et al. (2021). Here the actual modelling domain is of size 1200×1200 km, shown by the inner square with solid lines. The desired quantity is the Green’s function throughout this domain, due to a source at the receiver location marked by the inverted triangle. In the ANSEICCA implementation, an outer domain of size 2400×2400 km is used and the Green’s function calculated throughout it, for a source at the origin (red dot). The obtained solution is shown here in colour, at some arbitrary frequency. The desired quantity is then obtained by simply windowing this outer domain solution, using the square marked with dashed lines. This square is the same size as the actual domain, but is centred (open white circle) at the mirror image, with respect to the origin, of the actual receiver location. Thus by positioning the window appropriately, the solution can be obtained for a source at any location within the modelling domain.

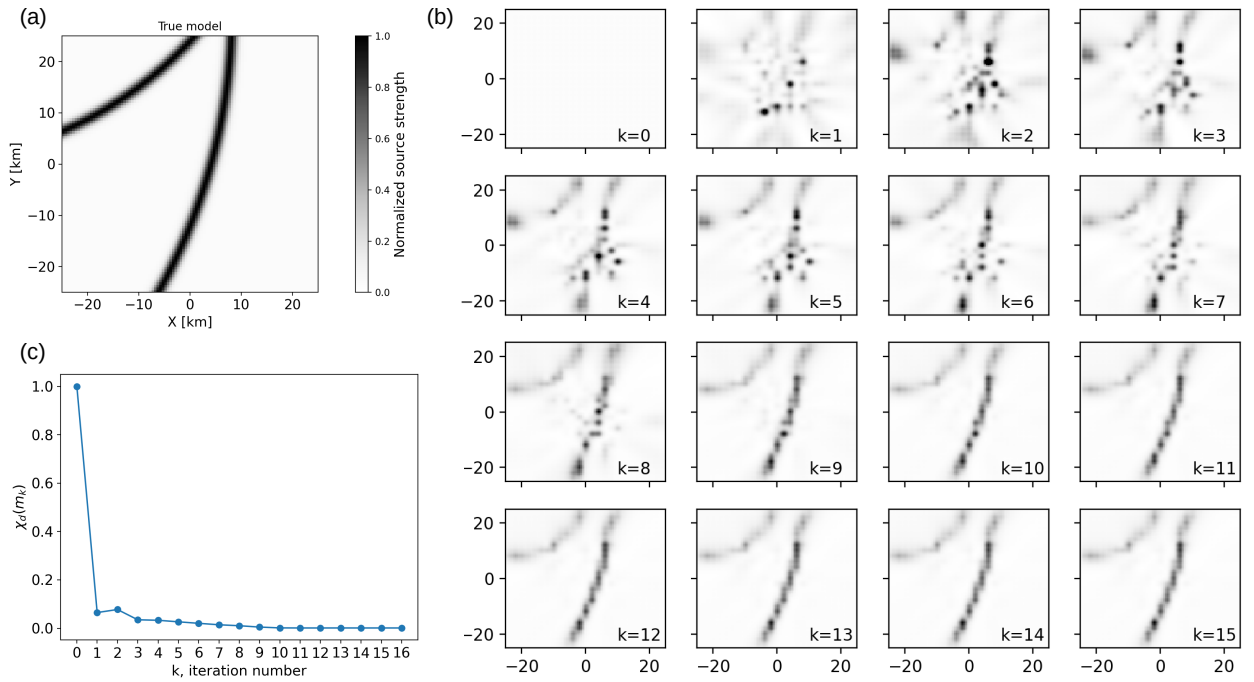


Figure 2: Synthetic test to illustrate inversion progress. (a) The test model for the E1 example; note that this is the same model as in Figure 2d of Datta et al. (2023). (b) Evolution of the model with progress of inversion (as indicated by the iteration number k in each panel); note the homogeneous starting model in the top left, and the inversion result in the bottom right. (c) Evolution of data misfit, showing $\approx 99\%$ misfit reduction in this synthetic example.

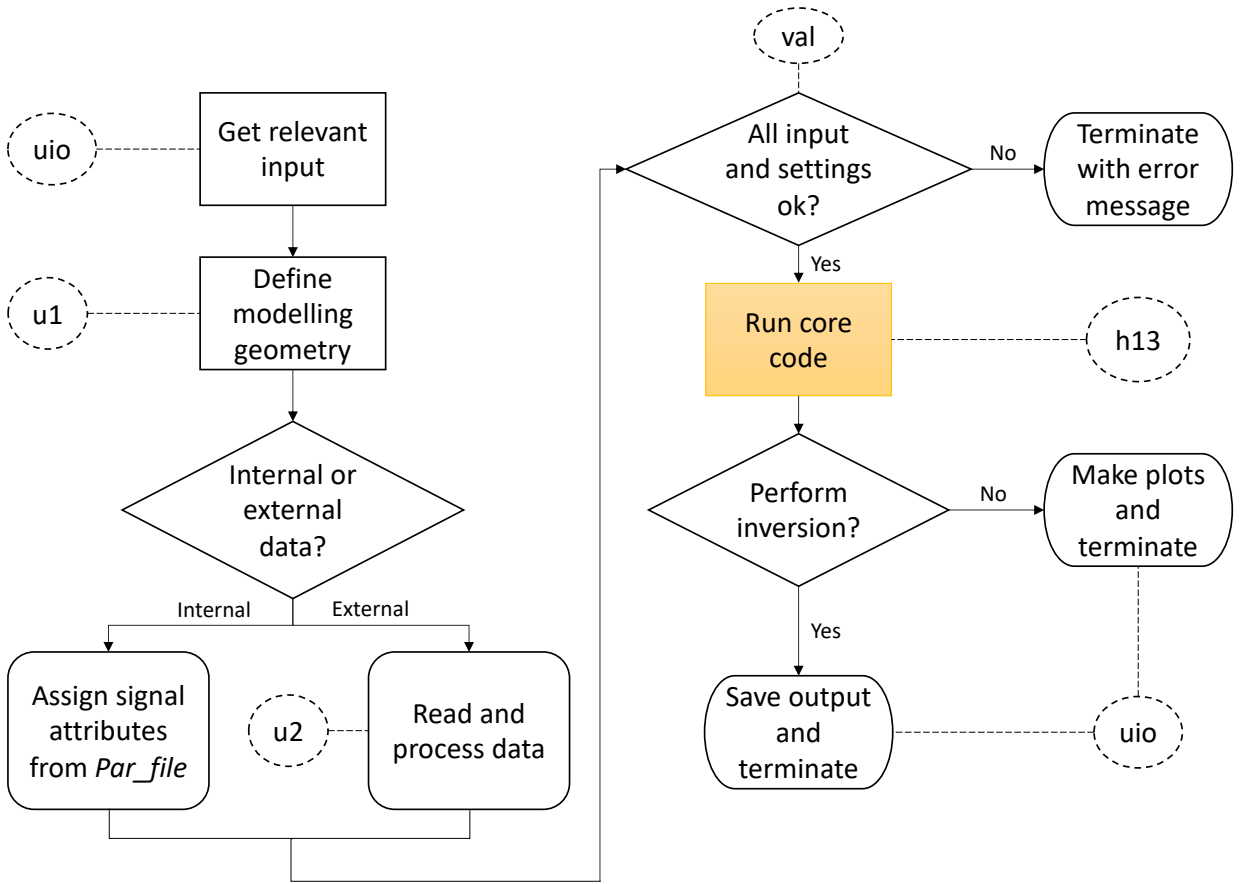


Figure 3: Flowchart of the overall structure of the package, essentially mirroring the wrapper programs. The highlighted (yellow) process in this flowchart is the one that is parallelised (see Section 3.3). The dashed circular inputs associated with any step or process represent the modules used for its implementation, as per the nomenclature of Table 3. We note that the *config* module is not shown here, but is used ubiquitously. See Section 3.2.1 for the definitions of ‘internal/external’ data.

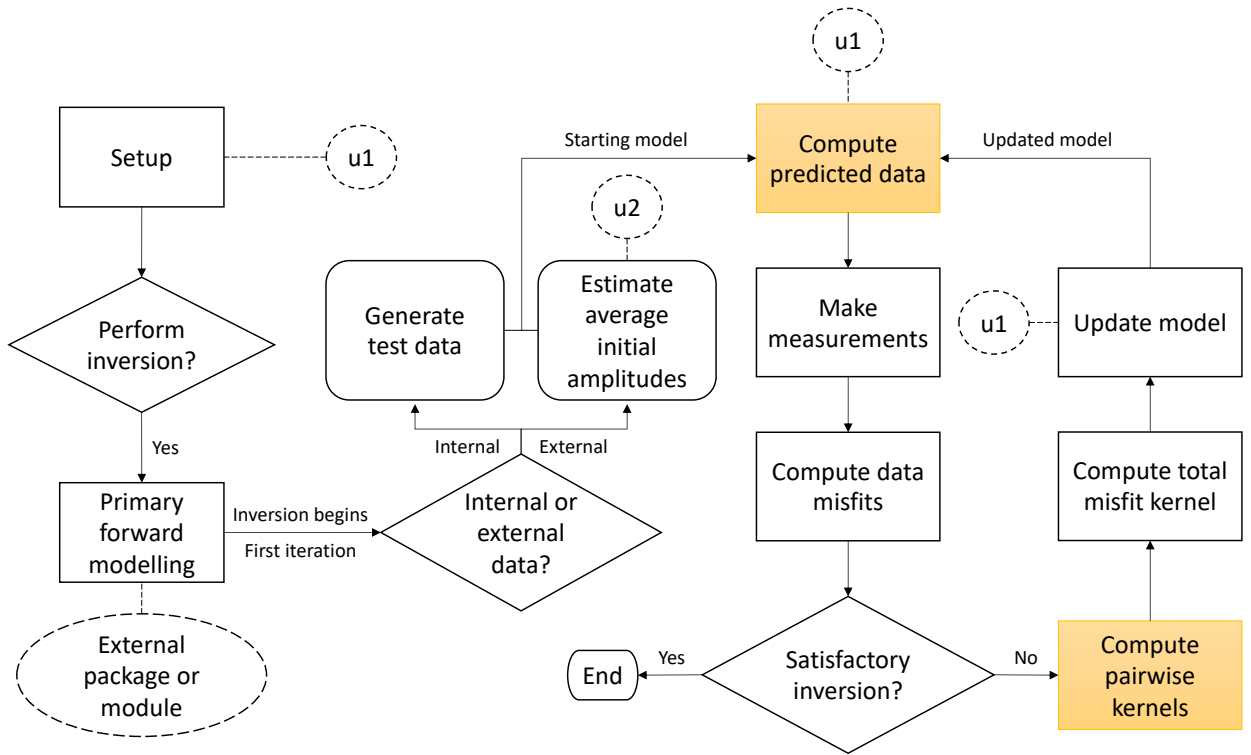


Figure 4: Flowchart showing the detailed structure of the core module, h13. The two highlighted boxes, which are part of the inversion loop, represent code operations that are parallelized. Other symbols have the same meaning as in Figure 3.

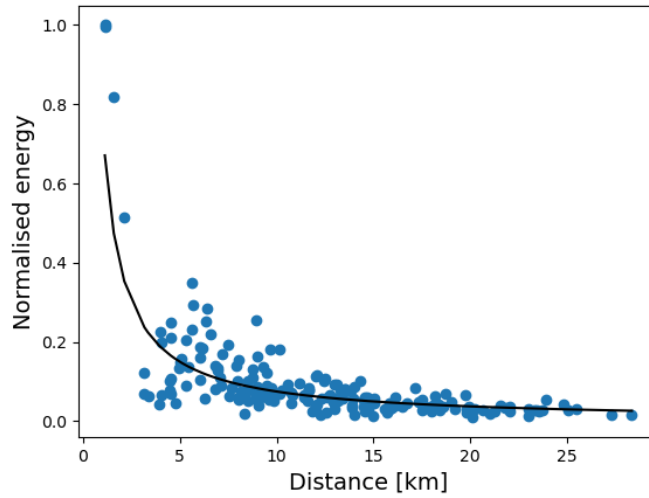


Figure 5: Example of curve-fitting for observed cross-correlation energy as a function of inter-receiver distance r , taken from the test data of example E1. The blue circles show the observed energies, and the black line is the best fitting $1/r$ curve. Energies are normalised with respect to the maximum observed value. First-iteration synthetics in an inversion will be scaled such that their energies match the black curve.

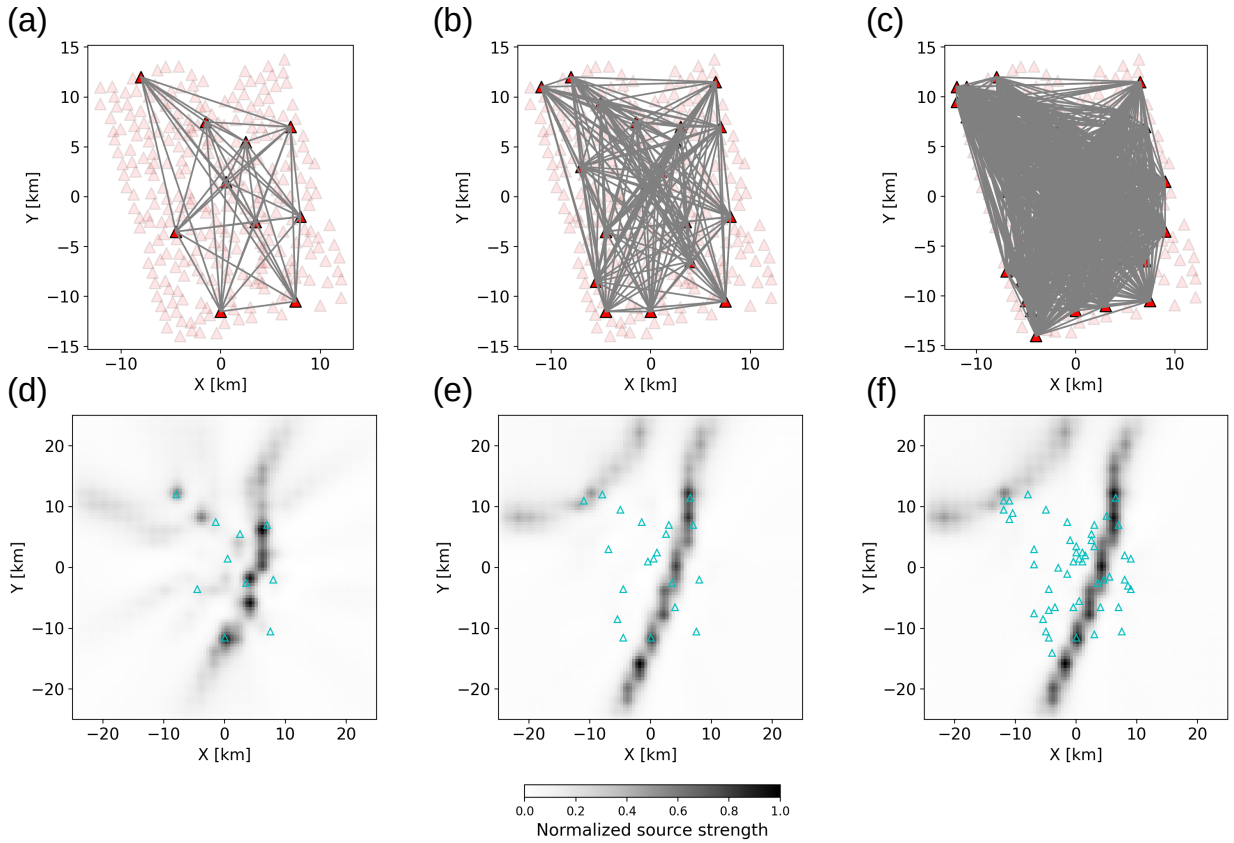


Figure 6: Inversion setup and results related to the benchmark tests. (a)-(c) Receiver maps showing the selection of 10, 20 and 50 receivers (dark red triangles), along with inter-receiver paths (grey lines). (d)-(f) Corresponding inversion results (after completion of all iterations) for a model size of 101×101 . Note that (b), (e) correspond to Figure 2.